THz-driven split ring resonator undulator

D. Rohrbach,[1,*] Z. Ollmann,[1] M. Hayati,[1] C. B. Schroeder,[2] W. P. Leemans,[3] and T. Feurer[1]

[1]*University of Bern, 3012 Bern, Switzerland*
[2]*Lawrence Berkeley National Laboratory, Berkeley 94720, California, USA*
[3]*Deutsches Elektronen-Synchrotron (DESY), 22607 Hamburg, Germany*

(Received 21 July 2020; accepted 11 January 2021; published 28 January 2021)

We propose a short period undulator based on the electromagnetic field pattern in a THz-driven split ring resonator structure. An analytical model is developed that allows us to assess the key performance parameters of the undulator and to estimate the emitted radiation spectrum. Different geometric configurations are compared in detail using numerical simulations. A 100 MeV electron bunch with 5 pC charge is shown to emit narrow band 83 eV photon pulses with a peak brightness of approximately 10^{19} photons/(s mrad^2 mm^2 0.1% BW) when passing through the 100 mm long undulator with a 1 mm period.

DOI: 10.1103/PhysRevAccelBeams.24.010703

I. INTRODUCTION

Undulators are generally composed of a periodic, alternating array of normal- or superconducting electromagnets, permanent magnets or hybrid magnets [1–3]. Relativistic electron bunches propagating through an undulator are forced on an oscillatory orbit, which leads to emission of intense narrow band radiation pulses [4]. The emission can range from THz to hard x-ray photon energies and is determined by electron kinetic energy and undulator period. Typical undulator periods are tens of millimeters, magnetic field strengths range from about one Tesla to more than ten Tesla for superconducting magnets, and undulators in free electron lasers can be tens to hundreds of meters in length [5,6].

Decreasing the undulator period is generally beneficial, because less electron energy is required to produce a given photon energy. Likewise, the emitted photon energy would increase for a given electron energy. In addition, smaller scale undulators in combination with miniaturized accelerators are suitable for the development of compact future light sources. Such advanced accelerators are for example based on laser wakefields in plasma [7] or laser-driven dielectric structures [8]. In the past, several efforts to reduce the periodicity of static magnetic field patterns have been made and values as low as 15 mm [9–12] were achieved. Further reduction down to about 100 μm was realized with laser micro-machined permanent magnets [13] or electromagnets [14]. The peak magnetic field in these devices was still as high as 0.7 T [15]. Usually, a shorter undulator period also requires a smaller undulator gap, which is ultimately limited by the transverse beam size, the radiation opening angle and the generated wakefields.

The undulator performance is mostly determined by the undulator parameter K which scales linearly with field strength and is proportional to the undulator period. Because optimal performance is achieved for an undulator parameter on the order of unity [4], a smaller undulator period would require a larger magnetic field. For example, a reduction of the undulator period to 1 mm already requires a magnetic field strength around 10 T. To the best of our knowledge, such field strength cannot be obtained by today's micromachined electromagnets. A conceptually different approach for a short period undulator uses oscillating electromagnetic fields, for example, in laser irradiated dielectric gratings [16], laser-driven undulators [17], microwave undulators [18], plasma wave undulators [19–21] or surface plasmon polariton (SPP) undulators [22–24].

Here, we propose a THz-driven undulator with a period of approximately 1 mm. It consists of an array of split ring resonators (SRRs) which locally enhance the THz driver field [25]. Similar structures have recently been used for electron deflection in streaking experiments [26–28]. Generally, the THz frequency range is of interest for electron bunch manipulations because the wavelength is well matched to the typical electron bunch size of several tens of microns. In comparison to THz-driven SPP undulators [24], SRR based undulators benefit from an order of magnitude larger field enhancement. In addition, wakefield effects are substantially reduced and the proposed undulator structure requires only one THz driver pulse (TDP).

A schematic of the proposed THz-driven SRR undulator is shown in Fig. 1. It is composed of C-shaped SRRs, which

*david.rohrbach@iap.unibe.ch

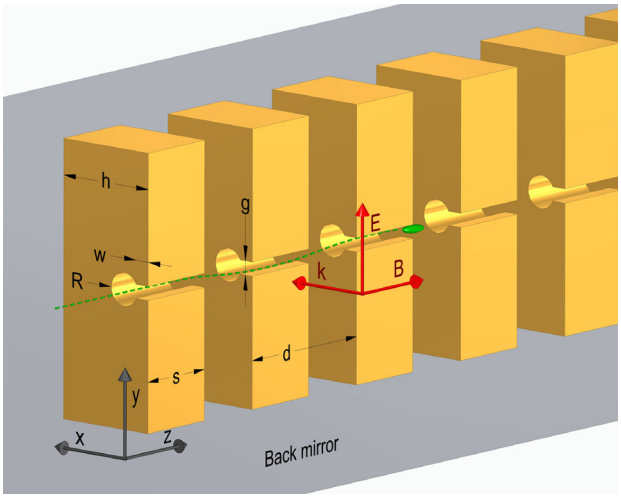

FIG. 1. Schematic of the THz-driven undulator: The electric field of the TDP (shown by red arrows) is enhanced inside the gap of the C-shaped SRRs. An electron bunch (green) propagating in positive z-direction, as indicated by the green dashed curve, is periodically deflected in $\pm y$-direction and as a result emits linearly polarized radiation.

are known to feature considerable field enhancement. In principle, other sub-wavelength structures with different resonance characteristics or field enhancement properties may be used [27,28]. Resonance frequency and field enhancement are mainly determined by geometry, namely by gap height g, gap width w and hole radius R (see Fig. 1 for the definition of the parameters). The TDP is linearly polarized along the y-direction and propagates in positive x-direction. It couples to the fundamental resonance of the SRR and leads to a locally enhanced electric field inside the gap. This field is relatively homogeneous and predominantly polarized in y-direction.

The electron bunches propagate through the SRR gaps in positive z-direction, as indicated by the green dashed curve, and interact with the electromagnetic fields. Due to the strong field enhancement, the electron dynamics is predominantly determined by the y-component of the in-gap electric field rather than any of the other electric or magnetic field components. By adjusting the SRR distance d to half of the free space resonance wavelength, the electrons are periodically deflected in $\pm y$-direction. Therefore, the optimal undulator period is directly linked to the resonance frequency of the SRR. The electron deflection pattern is further influenced by the filling factor $F := s/d$ of the SRR array. Note that for $F = 1$ the individual SRRs merge into a slotted tube. Here, we consider relativistic electron energies, which are of particular interest because of small radiation opening angles and lower wakefield instabilities.

II. CASE STUDY

In this section we present a case study of the SRR undulator concept with experimentally viable parameters. First, we define the undulator geometry and calculate the resonance condition as well as the electromagnetic fields via finite element simulations. Based on the simulations we derive an approximate analytic undulator model, which predicts the K-parameter and the emitted photon energies. Next, we study the dynamics of a single electron in a weak undulator field. Specifically, we study the emission spectrum as a function of the electron injection time relative to the TDP, initial transverse position, undulator periodicity and undulator filling factor. We conclude with electron bunch simulations, i.e., we simulate wakefields which allows us to specify upper limits for the bunch charge, we investigate the effect of stronger electromagnetic fields of the TDP and we study photon emission for two different (100 MeV and 1 GeV) electron beam energies.

A. Geometry

The SRR gap height g and width w are set to 50 μm, which is a good compromise to accommodate electron bunches with transverse sizes on the order of tens of microns while resulting in a close to homogeneous in-gap field distribution in x- and y-direction. The gap is at $x \in [-25\ \mu\text{m}, 25\ \mu\text{m}]$ and $y \in [-25\ \mu\text{m}, 25\ \mu\text{m}]$. The hole radius R is tuned for a resonance frequency of approximately 270 GHz, which corresponds to an undulator period of $2d = 1.1$ mm. The distance h is chosen such that the in-gap electric field at the resonance frequency is enhanced by the TDP reflected from the back mirror. The undulator length is arbitrarily set to $L = 100$ mm, but in practice is linked to the available THz source [29] as one has to maintain the desired electromagnetic field strength over the entire undulator length. We estimate the required THz energy, assuming a focal spot size of 100 mm by 1 mm, a pulse duration of 5 ps and a peak electric field strength of 10 MV/m, to approximately 70 μJ TDP energy, which is experimentally achievable with different types of THz sources [29–31]. Table I summarizes all the relevant dimensions of the SRR undulator.

B. Undulator fields

The spatial and temporal electric and magnetic field distributions of the SRR resonators were simulated with the

TABLE I. SRR undulator dimensions (see also Fig. 1 for the definition of parameters).

Parameter	Symbol	Value
Gap height	g	50 μm
Gap width	w	50 μm
Hole radius	R	60 μm
SRR thickness	s	50 μm–555 μm
SRR distance	d	555 μm
Filling factor	F	0.09–1
Distance to wall	h	390 μm
Undulator length	L	100 μm

finite-element software COMSOL [32]. The simulations were performed in three dimensions with periodic boundary conditions in z-direction and scattering boundary conditions in x- and y-directions. The permittivity of the SRR and the back mirror material was described by a Drude-model with a plasma frequency of 2.2 PHz and a damping rate of 6.4 THz (these parameter values have only minor influence on the field maps). The TDP was modeled by a plane wave. First, we performed frequency domain simulations to identify resonance, field enhancement and spatial distribution of the electric and magnetic fields at resonance. Then, we performed time-dependent simulations to determine the time dependence of the electric and magnetic fields when excited with a realistic TDP. For further simulations of the electron dynamics all six field maps at resonance were exported for a discrete grid with a maximum spacing of 2 μm, 1 μm and 5 μm in x-, y- and z-direction, respectively.

The simulations show that the in-gap resonance electric field is dominated by the enhanced y-component with negligible E_x and E_z contributions. The magnetic field is mostly in z-direction and concentrated in the circular SRR hole but decays into the gap region. The frequency dependent electric field enhancement was calculated as the volume average of E_y inside the SRR gap normalized to the electric field strength of the TDP.

Figure 2(a) shows the y-component of the electric field at resonance as a function of longitudinal position through the center of four SRR gaps (i.e., at $x = y = 0$ μm) and normalized to the electric field strength of the incident TDP. The thickness s was arbitrarily set to 300 μm. The inset shows the electric field amplitude E_y at the gap center versus x and y. Close to the center, it is rather homogeneous with some inhomogeneities at the edges of the gap. Figure 2(b) shows the Fourier decomposition of $E_y(z)$ at a fixed time, with a harmonic spectrum typical of the longitudinal, almost square electric field distribution.

Figure 2(c) shows a realistic TDP (red dash-dotted curve) and the excited in-gap y-component of the electric field (blue solid curve). The in-gap field oscillates for times longer that the impulsive excitation because the resonance linewidth is narrower than the excitation spectrum, as indicated in Fig. 2(d).

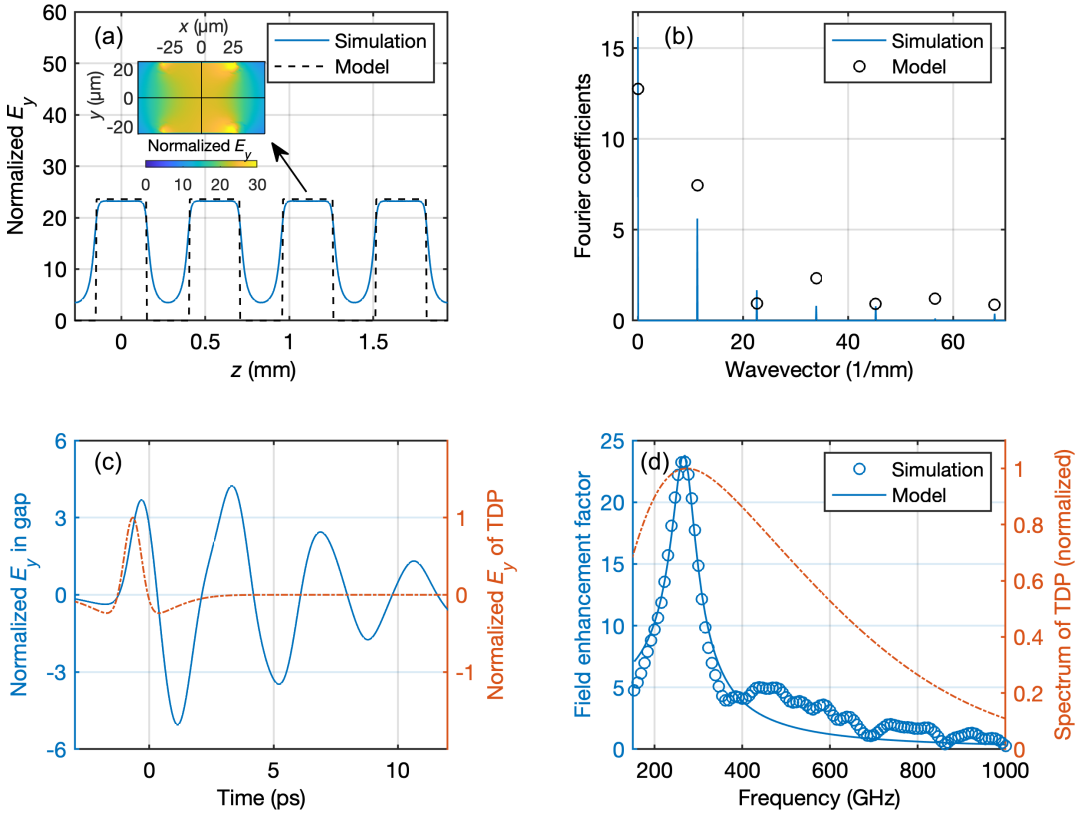

FIG. 2. (a) Simulated y-component of the electric field at the middle of the SRR gap as a function of the longitudinal position. The field is normalized to the electric field strength of the TDP and the time is fixed for the maximum field strength. The SRR thickness s is 300 μm and distance d is 555 μm. The black dashed curve corresponds to the assumption used in the analytic model Eq. (5). The inset shows the y-component of the electric field in a xy-slice at the longitudinal position of the gap middle. (b) Fourier spectrum of the longitudinally varying electric field together with the Fourier components from the analytic model Eq. (6). (c) Simulated time-dependent field inside the SRR gap exited by a specific TDP. (d) Spectrum of the TDP and the frequency dependent enhancement factor. The solid curve corresponds to a fit based on Eq. (2).

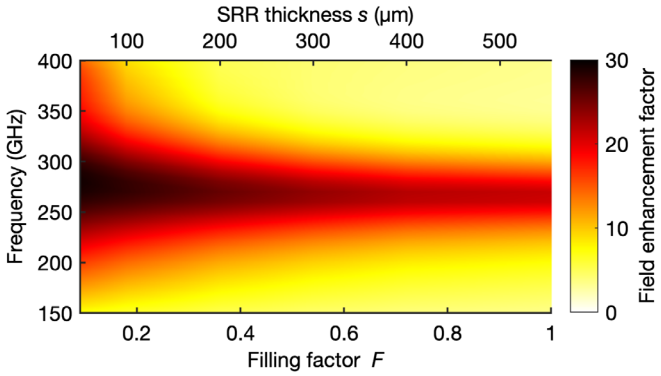

FIG. 3. Color-coded field enhancement $|\eta(\omega)|$ as a function of frequency and filling factor for a SRR array with a fixed distance of $d = 555$ μm.

Figure 3 shows the absolute value of the in-gap field enhancement factor as a function of frequency and filling factor. This figure shows that the resonance frequency of approximately 270 GHz is independent of the filling factor F. For the considered SRR thickness, which exceeds the skin depth, the full width at half maximum (FWHM) decreases from 190 GHz to 70 GHz for larger filling factors. Therefore, a realistic single-cycle TDP spectrum is broader than the resonance curve. The highest field enhancement of 29 is found for the structure with the smallest filling factor and can be attributed to the maximal field concentration and contribution from the reflected pulse.

C. Approximate analytic model

Here we derive an analytic model to estimate the undulator performance. In particular, we solve the Lorentz equation of motion for a single electron moving through the periodic deflection fields, and determine the K-parameter and the wavelength of the emitted radiation. The TDP spectrum $E_d(\omega)$ and the time varying electric field inside the SRR gap $E_{\mathrm{gap}}(t)$ are related via

$$E_{\mathrm{gap}}(t) = \Re\left\{\frac{1}{2\pi}\int_{-\infty}^{\infty} E_d(\omega)\eta(\omega)\mathrm{e}^{\mathrm{i}\omega t}d\omega\right\}, \tag{1}$$

where $\eta(\omega)$ is the frequency dependent complex field enhancement factor. Figure 2(d) shows that $\eta(\omega)$ can be well approximated by a Lorentz curve

$$\eta(\omega) = \frac{\eta_0}{\omega_0^2 - \omega^2 + \mathrm{i}\zeta\omega}, \tag{2}$$

where $f_0 = \frac{\omega_0}{2\pi}$ is the resonance frequency and ζ is the damping factor. The parameter η_0 determines the maximum field enhancement factor. In order to have oscillations the resonator must not be overdamped, which implies an upper limit of the damping factor. Since the TDP spectrum is much broader than the resonance curve, we can assume the TDP spectrum to be approximately constant in the frequency range of significant field enhancement. Therefore, at a time Δt after excitation with the TDP we find

$$E_{\mathrm{gap}}(\Delta t) \approx \frac{2|E_d(\omega_0)|\eta_0 \mathrm{e}^{-\zeta\Delta t/2}}{\sqrt{4\omega_0^2 - \zeta^2}} \sin\left(\frac{\Delta t}{2}\sqrt{4\omega_0^2 - \zeta^2}\right). \tag{3}$$

For small damping factors and at times close to the excitation (i.e., $\zeta \ll \omega_0$ and $\zeta\Delta t \ll 1$) the electric field inside the gap can be approximated by

$$E_{\mathrm{gap}}(t) \approx E_0 \sin(\omega_0 t + \varphi_0), \tag{4}$$

where φ_0 is an arbitrary phase and $E_0 := E_{\mathrm{THz}}|\eta(\omega_0)|$ with $E_{\mathrm{THz}} := |E_d(\omega_0)|\zeta$. Note that damping can also be neglected if a TDP with a tilted pulse front is employed. The tilt should be matched to the electron velocity [33–35]. Employing the Fourier decomposition of the z-dependent electric field we find

$$E_y(z,t) = E_0 \sin(\omega_0 t + \varphi_0) \sum_{n=-\infty}^{\infty} A_n \cos\frac{2\pi n z}{d}, \tag{5}$$

with the Fourier amplitudes of the harmonics A_n. In case we approximate the longitudinal field distribution by a square function, as shown in Fig. 2(a), the Fourier amplitudes can be estimated to

$$A_n := \begin{cases} F, & n = 0 \\ \frac{1}{\pi n}\sin \pi n F, & n \neq 0 \end{cases}. \tag{6}$$

For solving the equation of motion of a single electron, we assume $z(t) = \beta_{z0} ct$, where β_{z0} is the initial electron velocity in z-direction normalized to the speed of light in vacuum c. We further assume zero initial velocity in x- and y-direction and find

$$\begin{aligned} \gamma(t) &= \left[1 + (\gamma_0\beta_{z0})^2 + \left(\sum_{n=-\infty}^{\infty} K_n \cos\psi_n\right)^2\right]^{1/2} \\ \beta_z(t) &= \frac{\gamma_0}{\gamma(t)}\beta_{z0} \\ \beta_y(t) &= \frac{1}{\gamma(t)}\sum_{n=-\infty}^{\infty} K_n \cos\psi_n \end{aligned} \tag{7}$$

where γ_0 is the initial Lorentz factor,

$$K_n := \frac{eE_0 d A_n}{cm(d\omega_0 + 2\pi n c\beta_{z0})}, \tag{8}$$

and $\psi_n := (\omega_0 + \frac{2\pi c\beta_{z0} n}{d})t + \varphi_0$ for $n \in \mathbb{Z}$, where m is the electron rest mass and e the elementary charge. The assumption $z(t) = \beta_{z0} ct$ breaks down in the limit of large K_n-values, but it allows to find analytic expressions for relevant radiation properties. Note that K_0 is proportional to

the filling factor, because $A_0 \approx F$. For example, we find an undulator parameter of $K_0 \approx 0.07$ for a resonance frequency of 270 GHz, a filling factor of $F = 0.2$ and $E_0 = 1$ GV/m. By increasing the filling factor up to $F = 1$ the undulator parameter increases to $K_0 \approx 0.35$.

Based on the slippage condition, the emitted photon frequencies in the lab frame are given by

$$\omega_{r,n} = \frac{|\omega_0 + 2\pi\beta_{z0}cn/d|}{1 - \beta_{z0}\cos\theta} \tag{9}$$

where θ is the emission angle with respect to the z-axis. The best undulator performance is expected for a structure with $2\pi c/\omega_0 = \lambda_0 = 2d$, since the electric field inside the gap changes sign each time the bunch travels from one resonator to the next and yields an oscillatory motion with a period of $2d$. The on-axis photon frequencies are $2\gamma^2 ck_n$, with $k_n := |k_0(2n+1)|$ and $k_0 := \omega_0/c$, that is, the emission spectra consist of multiple odd higher harmonics.

The relative bandwidth of the emission mainly depends on the number of undulator periods and the relative energy spread of the electrons. The natural bandwidth of an undulator can be estimated by considering the Fourier transform limit of the radiation cycles [36]. At the resonance frequency f_0, the electrons oscillate $N_{u,n} = Lk_n/(2\pi)$ times (where L is the total undulator length) resulting in a relative bandwidth

$$\frac{\Delta\omega_{r,n}}{\omega_{r,n}} = \sqrt{(0.886/N_{u,n})^2 + (2\Delta E/E)^2}, \tag{10}$$

where $\Delta\omega_{r,n}$ is the FWHM of the on-axis spectral intensity and $\Delta E = 2\sqrt{2\ln 2}\sigma_E$ is the FWHM of the initial energy spread of the electrons (assuming a Gaussian energy distribution with standard deviation σ_E). Furthermore, the radiation is confined in a narrow emission cone with an opening angle of $\theta \approx 1/\gamma$ [4].

D. Single electron dynamics

In this section we consider a single electron with an initial energy of 100 MeV for the calculation of the electron trajectories and the emitted radiation spectra. The electron trajectories were calculated with VDSR (*virtual detector for synchrotron radiation*) [37] based on the three dimensional field maps from the frequency-domain COMSOL simulation. From the trajectories the intensity of the emitted radiation per frequency interval and per solid angle in the far field is calculated [38]

$$\frac{\mathrm{d}^2 I}{\mathrm{d}\omega\mathrm{d}\Omega} = \frac{e^2}{16\pi^3\varepsilon_0 c}\left|\int_{-\infty}^{\infty}\frac{\hat{\mathbf{n}}_r \times [(\hat{\mathbf{n}}_r - \beta)\times\dot{\beta}]}{(1-\hat{\mathbf{n}}_r\beta)^2} \times \exp\left(i\omega\left(t - \frac{\hat{\mathbf{n}}_r\mathbf{r}}{c}\right)\right)\mathrm{d}t\right|^2 \tag{11}$$

where $\hat{\mathbf{n}}_r$ is a unit vector pointing in the observation direction. From the simulated on-axis spectra we estimate the radiation peak brightness using the peak intensity (in units of photons/(sr 0.1%BW)) divided by the bunch duration $2\sigma_z/c$ and the bunch cross section area $\pi\sigma_r^2$.

The SRR thickness is set to $s = 100$ μm and the incident peak THz electric field is $E_{\mathrm{THz}} = 1$ MV/m. Note that for high undulator field strengths the net deflection can be as large as the gap size and the electron may collide with the SRRs.

A consequence of time dependent undulator fields is that the time delay between the TDP and the electron injection into the structure is crucial. The exact injection time determines the overall deflection in y-direction as well as the emitted radiation intensity. Note that the deflection in x-direction is negligible irrespective of injection time. Figure 4 shows the y-deflection at the end of the undulator and emitted peak intensity versus time delay between TDP and electron injection.

An electron injected at zero time delay, or at an integer multiple of half the oscillation period, reaches the SRR gap when the field strength is at its maximum resulting the highest peak intensity. Note that this corresponds to $\varphi_0 = \pi/2$ in Eq. (4). If the electron has no initial momentum in y-direction, a net deflection arises which is determined by the first momentum kick at the undulator entrance. As a consequence, the emission cone bends away from the z-axis. If the time delay is adjusted such that the electron passes the gap when the deflection field has a zero-crossing, the net deflection is zero but also the peak intensity is minimal. To avoid a net deflection while maintaining the time delay for maximum emitted intensity we propose to compensate the deflection with a matched initial momentum in y-direction. For the simulation parameters used here, we found that an initial normalized y-momentum of 0.004 can balance the net deflection at zero time delay. In the following the initial y-momentum is always adjusted for zero net deflection. Such initial y-momentum can be achieved with a standard undulator end design, here for example with the first SRR having only

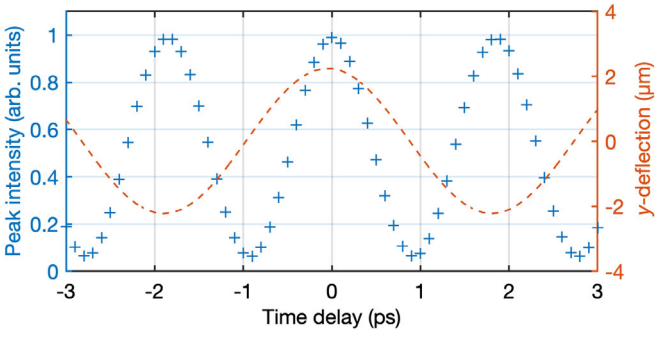

FIG. 4. Simulated on-axis peak intensity and total deflection in y-direction as a function of time delay between electron injection and TDP.

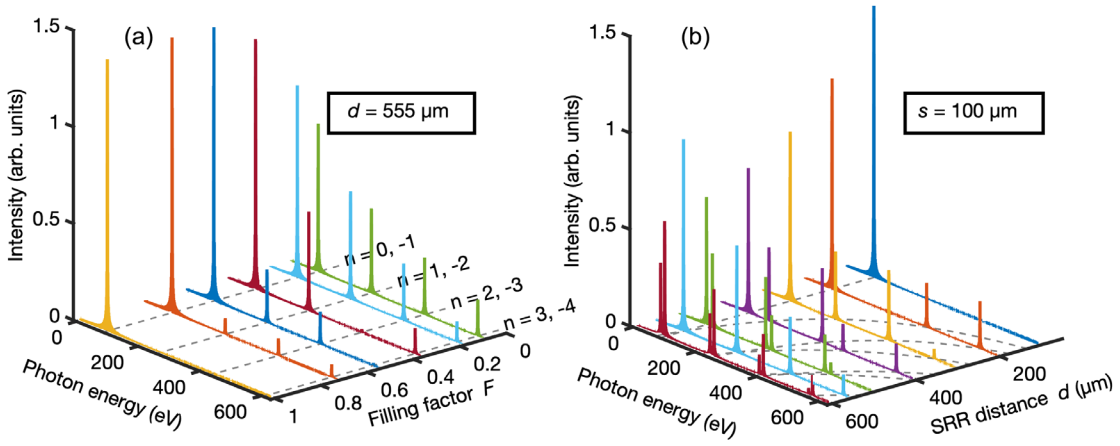

FIG. 5. Simulated on-axis spectra and the predicted photon energies based on the analytic model (gray dashed curves) for different filling factors (a) and distances (b). Geometries for six different filling factors (a) and for seven different SRR distances (b) were considered.

half the thickness s or a larger width w for reducing the deflection field strength at the undulator entrance [4].

The emitted radiation spectra can be tuned by adjusting the SRR distance d and the filling factor F. Figure 5 summarizes the simulated on-axis radiation spectra for different parameters. Note that all structures have the same resonance frequency of 270 GHz. The gray dashed curves show the predicted photon energies based on Eq. (9) for the corresponding harmonics n. In Fig. 5(a) we show the spectra for different filling factors F but for a fixed distance of 555 μm. Because the distance is matched to the resonance frequency each emission peak has contributions from two Fourier components A_n as indicated by the corresponding values of n. For increasing F we found an increased emission intensity at the photon frequency $\omega_{r,0}$ (which corresponds to 86.4 eV). This is explained by the increased interaction time between the electric field and the electrons. For increasing F, the higher order harmonics diminish, as it is expected based on the corresponding Fourier coefficients A_n. In the limit of a slotted tube, i.e., $F = 1$, no harmonics are generated, which is in agreement with $A_n = 0$ for $n \neq 0$. For small filling factors, multiple emission lines occur at odd higher harmonics.

On the other hand, in Fig. 5(b), we fixed the SRR thickness to 100 μm but changed the distance between resonators. Again we find good agreement between simulated emission peaks and analytic model. The highest emission intensity is obtained when the distance is matched to the resonance frequency ($d = 555$ μm) or when the SRRs are closely spaced such that the structure approaches a slotted tube. Likewise, the photon energy of the higher order harmonics can be tuned over a wide range by adjusting the SRR distance. Also here, the resulting emission intensities are governed by the Fourier coefficients A_n.

Any inhomogeneity of the undulator fields in the gap area could potentially effect the undulator performance. Therefore we compare the radiation spectra for different initial x-positions x_0 as shown in Fig. 6. While the emitted photon energy is unchanged, the intensity decreases when the electron travels off-axis. Note that the intensity is still more than 60% of the on-axis intensity even if the electron travels alongside the SRR gap. Since the deflection field is not entirely symmetric in x-direction, the emission intensities for $x_0 = -30$ μm and $x_0 = 30$ μm are slightly different. The analytic model in Eq. (9) predicts a photon energy of 86.4 eV (shown as black dashed line), which is in agreement with the simulation results.

E. Electron bunch dynamics

In the following, we discuss the dynamics of an electron bunch, rather than a single particle, interacting with the undulator fields. A undulator structure with $s = 300$ μm and $d = 555$ μm is considered, but similar results are obtained for different filling factors. The kinetic energy of the bunch was fixed to 100 MeV and we assumed a relative energy spread of 1%, as provided by todays accelerators [39]. The total bunch charge is 5 pC with a Gaussian distribution and standard deviations $\sigma_r = 5$ μm

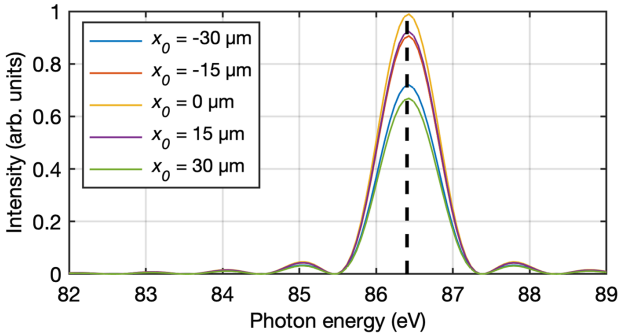

FIG. 6. Simulated on-axis spectra for different initial x-positions.

TABLE II. Electron bunch parameters considered in the numerical simulations.

Parameter	Symbol	Value
Kinetic energy	E	100 MeV
Relative energy spread	σ_E/E	1%
Bunch charge	Q	5 pC
Transverse size	σ_r	5 μm
Longitudinal size	σ_z	20 μm

and $\sigma_z = 20$ μm in transverse and longitudinal direction. Table II summarizes the electron bunch parameters. For simplicity, we set the emittance to zero, that is, the electrons have no initial momentum spread in the x- and y-direction. If required, the maximum allowed emittance can be estimated by setting the maximum transverse bunch size equal to the gap size and by using a beta function determined by the undulator length L. As a result, the geometric emittance must be much smaller than $g^2/(4L) = 6.3$ nm rad which corresponds to a normalized emittance of 1.2 μm rad.

The electron bunch will generate its own wakefield when propagating through the SRR structure. In the worst case this undesirable wakefield can lead to substantial beam degradation. Therefore the wakefield limits the total allowed bunch charge and/or the minimum beam energy. Figure 7 shows the simulated on-axis longitudinal wake potential, which generally leads to an energy loss of the electrons and therefore to an increasing energy spread. We simulated wakefields with the finite-element software CST [40], where the electron bunch was approximated by a line current with a longitudinal Gaussian distribution with standard deviation σ_z. Ideally, the integration of the wakefields is performed over the whole structure length, which was not feasible due to long computation times. Therefore, just a fraction of the structure was considered and the wake potential per SRR was calculated (i.e., the simulated wake potential divided by the number of SRRs used in the simulation). The number of considered SRRs was increased until convergence is reached, which is usually 5 SRRs.

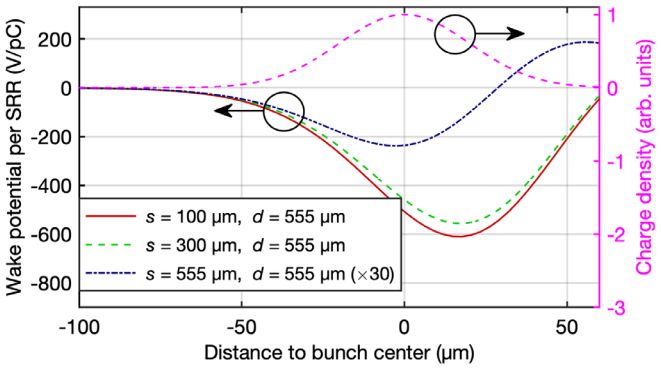

FIG. 7. Simulated on-axis wake potential per SRR normalized to the bunch charge as a function of distance to the bunch center (negative values refer to positions at the bunch front). For better visualization, the wake potential for a structure with $s = d = 555$ μm is multiplied by a factor of 30. The longitudinal bunch charge density with $\sigma_z = 20$ μm is shown as pink dashed curve.

The wakefield is zero at the head of the bunch and increases toward the tail. Because the slotted tube structure has no longitudinal corrugation, its wake potential is much smaller. For better visualization the wake potential of this structure is multiplied by a factor of 30 as indicated in the legend. For the other two structures we found a wake potential per SRR with a maximum amplitude of approximately 600 V/pC. Therefore, the maximum energy loss in a 100 mm long undulator which consists of 180 SRRs would be 110 keV/pC. For a beam energy of 100 MeV one would be limited to bunch charges smaller than approximately 5 pC, if one claims an energy loss of less than 1%. Note that for the slotted tube structure and the same beam energy, the bunch charge can reach 300 pC while the wakefield induced energy loss is still less than 1%.

The radiation spectra generated by an electron bunch was calculated by incoherently adding all spectra of the 1000 macro-particles, which were used for representing the bunch. Figure 8 shows the simulated on-axis spectra for different THz electric field strength E_{THz}. Recall that increasing the THz field strength should improve the undulator performance since the undulator parameter K approaches unity, and also the peak intensity is proportional to E_{THz}^2. The relative bandwidth of 5% is in good agreement with the theoretical bandwidth Eq. (10). For a classical undulator the relative bandwidth is typically around 0.7% [41]. In order to achieve a similar value for the SRR undulator, the energy spread must be reduced to 0.1% and the undulator length must be increased to 200 mm. For the highest THz field strengths, before the wiggling motion becomes similar to the gap size, we observe a red shift of the emitted spectra, which is a consequence of the decreased average velocity in z-direction. For $E_{\mathrm{THz}} = 40$ MV/m (which corresponds to an electric field strength of approximately 900 MV/m inside the gap) we find a peak intensity of 10^9 photons/(sr 0.1% BW) which

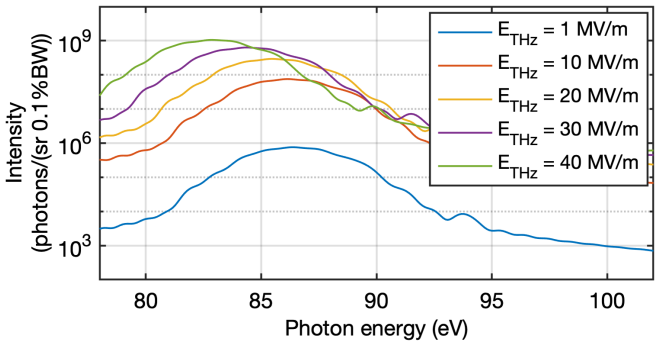

FIG. 8. On-axis spectra for bunches with 100 MeV energy, 5 pC charge, 1% relative energy spread and for different THz electric field strength.

corresponds to peak brightness of 10^{19} photons/(s mrad^2 mm^2 0.1% BW). The electric field strength is ultimately limited by the breakdown threshold of the SRR material. To the best of our knowledge, there is no measurement of the gold breakdown threshold in the THz range. However, based on experiment with nano-gap SRRs, we can confirm that the breakdown threshold exceeds 8 GV/m.

Due to wakefield instabilities the kinetic energy of 100 MeV should be regarded as a lower limit. However, we may increase the kinetic energy to the operation regime of recently commissioned XFELs of several GeV. An increase in kinetic energy causes the emitted photon energy to grow as γ^2 and the emission opening angle to shrink as $1/\gamma$. As an example we consider a beam energy of 1 GeV and a TDP peak electric field of $E_{\mathrm{THz}} = 40$ MV/m while all the other parameters remain as summarized in Tab. II. The emitted photon energy increases to 8.2 keV with a peak brightness of 10^{21} photons/(s mrad^2 mm^2 0.1% BW). Therefore, depending on the electron energy the undulator can operate from the UV to the hard x-ray range.

III. CONCLUSIONS

A new type of short period undulator is proposed, which is based on a SRR array structure driven by a THz pulse. Undulator periods around 1 mm with a deflection electric field strength of 1 GV/m are experimentally achievable. The corresponding undulator parameter K is approximately 0.3 and could be further increased toward unity depending on the available THz source. Due to its compact size the whole undulator structure could be directly installed in the vacuum beam tube. Propagating a 100 MeV electron bunch with 5 pC charge through a 100 mm long undulator driven by a state-of-the-art THz source was shown to emit 83 eV photons with a peak brightness of 10^{19} photons/(s mrad^2 mm^2 0.1% BW). For a 1 GeV bunch, the photon energy increases to 8.2 keV with a peak brightness of 10^{21} photons/(s mrad^2 mm^2 0.1% BW). Also higher order harmonic emission occurs whose intensity can be tuned by varying the filling factor or the SRR distance. Hence, the undulator can also act as a frequency comb. In comparison with the previously proposed SPP based THz undulator [24], the new concept benefits from a higher field enhancement and also reduces wakefield effects. Therefore it is a promising candidate for a low cost and compact radiation source, which produces directional, linearly polarized and narrow band radiation pulses in the UV to x-ray range. By combining the proposed undulator with a miniaturized advanced accelerator, a table top x-ray source is within reach. Such a source could find application in radiotherapy, ultrafast x-ray diffraction experiments or time-resolved x-ray spectroscopy.

Investigating alternative resonator structures could further improve the undulator performance. In general, structures with an increased gap area, a higher field enhancement or a shorter undulator period would be beneficial. A larger gap area would reduce the restrictions on the electron beam emittance, while an additional increase in field enhancement would further lower the demand on the TDP. A smaller periodicity would miniaturize the device even more and would reduce the kinetic energy requirement for producing a fixed photon energy.

ACKNOWLEDGMENTS

D. R., Z. O., M. H., and T. F. acknowledge funding from the Swiss National Science Foundation (SNSF) under Grant no. 200020-178812. Work at LBNL was supported by the U.S. Department of Energy under Contract No. DE-AC02-05CH11231.

[1] C. Pellegrini, A. Marinelli, and S. Reiche, The physics of x-ray free-electron lasers, Rev. Mod. Phys. **88**, 015006 (2016).

[2] J. M. Madey, Stimulated emission of bremsstrahlung in a periodic magnetic field, J. Appl. Phys. **42**, 1906 (1971).

[3] D. A. G. Deacon, L. R. Elias, J. M. J. Madey, G. J. Ramian, H. A. Schwettman, and T. I. Smith, First Operation of a Free-Electron Laser, Phys. Rev. Lett. **38**, 892 (1977).

[4] J. A. Clarke, *The Science and Technology of Undulators and Wigglers* (Oxford University Press, New York, 2004), https://oxford.universitypressscholarship.com/view/10.1093/acprof:oso/9780198508557.001.0001/acprof-9780198508557.

[5] V. S. Paul Scherrer Institute (PSI), SwissFEL - Conceptual design report, Tech. Rep. (Paul Scherrer Institute, Switzerland, 2010), https://inis.iaea.org/search/search.aspx?orig_q=RN:42006326.

[6] LCLS Parameters, https://portal.slac.stanford.edu/sites/lclscore_public/Accelerator_Physics_Published_Documents/LCLS-parameters-3-22-17.pdf.

[7] E. Esarey, C. B. Schroeder, and W. P. Leemans, Physics of laser-driven plasma-based electron accelerators, Rev. Mod. Phys. **81**, 1229 (2009).

[8] R. J. England *et al.*, Dielectric laser accelerators, Rev. Mod. Phys. **86**, 1337 (2014).

[9] J.-C. Huang, H. Kitamura, C.-K. Yang, C.-H. Chang, C.-H. Chang, and C.-S. Hwang, Challenges of in-vacuum and cryogenic permanent magnet undulator technologies, Phys. Rev. Accel. Beams **20**, 064801 (2017).

[10] H. Hsieh, S. Krinsky, A. Luccio, C. Pellegrini, and A. Van Steenbergen, Wiggler, undulator and free electron laser radiation sources development at the national synchrotron light source, Nucl. Instruments Methods Phys. Res. **208**, 79 (1983).

[11] W. Gudat, J. Pflüger, J. Chatzipetros, and W. Peatman, An undulator/multipole wiggler for the BESSY storage ring, Nucl. Instrum. Methods Phys. Res., Sect. A **246**, 50 (1986).

[12] S. Yamamoto, T. Shioya, M. Hara, H. Kitamura, X. W. Zhang, T. Mochizuki, H. Sugiyama, and M. Ando, Construction of an invacuum type undulator for production of

undulator x rays in the 5–25 keV region, Rev. Sci. Instrum. **63**, 400 (1992).

[13] B. A. Peterson, O. D. Oniku, W. C. Patterson, D. Le Roy, A. Garraud, F. Herrault, N. M. Dempsey, D. P. Arnold, and M. G. Allen, Technology Development for Short-period Magnetic Undulators, Phys. Procedia **52**, 36 (2014).

[14] J. Harrison, A. Joshi, Y. Hwang, O. Paydar, J. Lake, P. Musumeci, and R. N. Candler, Surface-micromachined electromagnets for 100 μm-scale undulators and focusing optics, Phys. Procedia **52**, 19 (2014).

[15] J. Harrison, A. Joshi, J. Lake, R. Candler, and P. Musumeci, Surface-micromachined magnetic undulator with period length between 10 μm and 1 mm for advanced light sources, Phys. Rev. Accel. Beams **15**, 070703 (2012).

[16] T. Plettner and R. L. Byer, Proposed dielectric-based microstructure laser-driven undulator, Phys. Rev. Accel. Beams **11**, 030704 (2008).

[17] F. Toufexis, T. Tang, and S. G. Tantawi, A 200 μm-period laser-driven undulator, *Proc. 36th Int. Free. Laser Conf.* (JACoW, Geneva, 2014), p. 131, https://accelconf.web.cern.ch/FEL2014/papers/mop047.pdf.

[18] S. Tantawi, M. Shumail, J. Neilson, G. Bowden, C. Chang, E. Hemsing, and M. Dunning, Experimental Demonstration of a Tunable Microwave Undulator, Phys. Rev. Lett. **112**, 164802 (2014).

[19] S. Corde and K. T. Phuoc, Plasma wave undulator for laser-accelerated electrons, Phys. Plasmas **18**, 033111 (2011).

[20] R. L. Williams, C. E. Clayton, C. Joshi, and T. C. Katsouleas, Studies of classical radiation emission from plasma wave undulators, IEEE Trans. Plasma Sci. **21**, 156 (1993).

[21] S. G. Rykovanov, C. B. Schroeder, E. Esarey, C. G. R. Geddes, and W. P. Leemans, Plasma Undulator Based on Laser Excitation of Wakefields in a Plasma Channel, Phys. Rev. Lett. **114**, 145003 (2015).

[22] L. J. Wong, I. Kaminer, O. Ilic, J. D. Joannopoulos, and M. Soljačić, Towards graphene plasmon-based free-electron infrared to X-ray sources, Nat. Photonics **10**, 46 (2016).

[23] G. Rosolen, L. J. Wong, N. Rivera, B. Maes, and M. Soljačić, and I. Kaminer, Metasurface-based multi-harmonic free-electron light source, Light. Sci. Appl. **7**, 64 (2018).

[24] D. Rohrbach, C. B. Schroeder, A. Pizzi, R. Tarkeshian, M. Hayati, W. P. Leemans, and T. Feurer, THz-driven surface plasmon undulator as a compact highly directional narrow band incoherent x-ray source, Phys. Rev. Accel. Beams **22**, 090702 (2019).

[25] K. Ji-Hun, K. Dai-Sik, and S. Minah, Terahertz wave interaction with metallic nanostructures, Nanophotonics **7**, 763 (2018).

[26] I. H. Baek, H. W. Kim, Y. C. Kim, M. Kim, S. J. Park, K. Y. Oang, K. Jang, K. Lee, Y. U. Jeong, N. Vinokurov, and T. Feurer, Terahertz activities at KAERI ultrafast electron diffraction facility, in *2018 43rd Int. Conf. Infrared, Millimeter, Terahertz Waves* (IEEE, Nagoya, 2018), pp. 1–2, https://ieeexplore.ieee.org/document/8510096.

[27] L. Zhao *et al.*, Terahertz Streaking of Few-Femtosecond Relativistic Electron Beams, Phys. Rev. X **8**, 021061 (2018).

[28] X. L. Shen, E. C. Snively, J. G. Navarro, D. Cesar, and P. Musumeci, A THz driven split-ring resonator based ultrafast relativistic electron streak camera, AIP Adv. **9**, 085209 (2019).

[29] J. A. Fülöp, S. Tzortzakis, and T. Kampfrath, Laser-Driven Strong-Field Terahertz Sources, Adv. Opt. Mater. **8**, 1900681 (2020).

[30] F. Ahr, S. W. Jolly, N. H. Matlis, S. Carbajo, T. Kroh, K. Ravi, D. N. Schimpf, J. Schulte, H. Ishizuki, T. Taira, A. R. Maier, and F. X. Kärtner, Narrowband terahertz generation with chirped-and-delayed laser pulses in periodically poled lithium niobate, Opt. Lett. **42**, 2118 (2017).

[31] L. Wang, A. Fallahi, K. Ravi, and F. Kärtner, High efficiency terahertz generation in a multi-stage system, Opt. Express **26**, 29744 (2018).

[32] COMSOL Multiphysics, https://www.comsol.com (2019).

[33] T. Feurer, J. C. Vaughan, and K. A. Nelson, Spatiotemporal coherent control of lattice vibrational waves, Science **299**, 374 (2003).

[34] S. Akturk, X. Gu, E. Zeek, and R. Trebino, Pulse-front tilt caused by spatial and temporal chirp, Opt. Express **12**, 4399 (2004).

[35] L. J. Wong and I. Kaminer, Ultrashort tilted-pulse-front pulses and nonparaxial tilted-phase-front beams, ACS Photonics **4**, 2257 (2017).

[36] P. Schmüser, M. Dohlus, J. Rossbach, and C. Behrens, *Free-Electron Lasers in the Ultraviolet and X-Ray Regime* (Springer International Publishing, Cham, Heidelberg, New York, Dordrecht, London, 2014), https://link.springer.com/book/10.1007%2F978-3-319-04081-3.

[37] M. Chen, E. Esarey, C. G. R. Geddes, C. B. Schroeder, G. R. Plateau, S. S. Bulanov, S. Rykovanov, and W. P. Leemans, Modeling classical and quantum radiation from laser-plasma accelerators, Phys. Rev. Accel. Beams **16**, 030701 (2013).

[38] J. D. Jackson, *Classical electrodynamics*, 3rd ed. (Wiley, New York, NY, 1999), http://cdsweb.cern.ch/record/490457.

[39] Sparc Parameters, https://www.lnf.infn.it/acceleratori/sparc/parameters.html (2019).

[40] CST - Computer Simulation Technology, https://www.3ds.com/de/produkte-und-services/simulia/produkte/cst-studio-suite/.

[41] Undulators at SLS, https://www.psi.ch/de/insertion-devices/sls.